
TRIPARTITE QUANTUM CORRELATIONS OBTAINED BY POST-SELECTION FROM TWIN BEAMS

Pavel Pavlíček

Institute of Physics of the Czech Academy of Sciences,
Joint Laboratory of Optics of Palacky University and Institute of Physics of CAS,
17. listopadu 50a, 779 00 Olomouc, Czech Republic
Pavel.Pavliceck@upol.cz

Jan Peřina Jr.

Joint Laboratory of Optics of Palacký University and Institute of Physics of CAS,
Faculty of Science, Palacký University,
17. listopadu 12, 779 00 Olomouc, Czech Republic
Jan.Perina.Jr@upol.cz

Václav Michálek

Institute of Physics of the Czech Academy of Sciences,
Joint Laboratory of Optics of Palacky University and Institute of Physics of CAS,
17. listopadu 50a, 779 00 Olomouc, Czech Republic
Vaclav.Michalek@upol.cz

Radek Machulka

Institute of Physics of the Czech Academy of Sciences,
Joint Laboratory of Optics of Palacky University and Institute of Physics of CAS,
17. listopadu 50a, 779 00 Olomouc, Czech Republic
Radek.Machulka@upol.cz

Ondřej Haderka

Joint Laboratory of Optics of Palacký University and Institute of Physics of CAS,
Faculty of Science, Palacký University,
17. listopadu 12, 779 00 Olomouc, Czech Republic
Ondrej.Haderka@upol.cz

January 21, 2026

ABSTRACT

Spatially-resolved photon counting of a twin beam performed by an iCCD camera allows for versatile tailoring the properties of the beams formed by parts of the original twin beam. Dividing the idler beam of the twin beam into three equally-intense parts and post-selecting by detecting a given number of photocounts in the whole signal beam we arrive at the idler fields exhibiting high degrees of nonclassicality and being endowed with tripartite quantum correlations. Nonclassicality is analyzed with the help of suitable nonclassicality witnesses and their corresponding nonclassicality depths. Suitable parameters are introduced to quantify quantum correlations. These parameters are analyzed as they depend on the field intensity. The experimental photocount histograms are reconstructed by the maximum-likelihood approach and the obtained photon-number distributions are compared with a suitable model in which the original twin beam is approximated by an appropriate multi-mode Gaussian field and undergoes the corresponding beams' transformations.

Keywords Spontaneous parametric down-conversion; Twin-beam; Three-mode correlations, Photon-number anti-correlations, Nonclassicality

1 Introduction

A twin beam (TWB) is formed by a pair of correlated light beams generated in the process of spontaneous parametric down-conversion or in the process of nonlinear optical amplification. [1]. The constituting beams are historically referred to as the signal and idler beams. Twin beams are endowed with nonclassical properties. [2] They exhibit the entanglement between the signal and idler beams. The entanglement originates in the correlation in the number of photons, entanglement also arises in the beams' polarization, spectral correlations, and tight spatial correlations. [3, 4, 5, 6, 7]

Twin beams are suitable for generating the states with the sub-Poissonian distribution using the post-selection process. Post-selection is performed based on the detection of a given number of photons in one of the two beams. [6, 8, 9, 10, 11, 12, 13, 14] The states with sub-Poissonian distribution are useful for quantum measurements as well as quantum imaging with the errors being below the standard quantum limit. [15, 16]

The post-selection process can be applied to more complex fields composed of several TWBs in different configurations. It is shown in Ref. [17, 18] that a two-beam field with anti-correlations in photon-number fluctuations and marginal sub-Poissonian photon-number distributions is left in the idler beams of two TWBs sharing their signal beams after post-selection that is based on the measurement of a given number of photocounts in their common signal beam. This result poses the question whether the sub-Poissonianity of the marginal beams and the mutual anti-correlations in photon-number fluctuations also occur in more general, complex, TWB configurations. Here, we answer this question by considering a straightforward generalization of the above configuration in which three TWBs share their signal beams for common photon detection and analyze the properties of the three idler beams emerging after post-selection conditioned by detecting a given number of common signal photocounts. We note that, in our experiment, we do not exploit the entanglement in polarization or spatial correlations between the beams. We only rely on the correlations in the number of photons between the signal and the idler beams. In our experiment, we divide the idler beam into three parts in which the photon numbers are independently measured. On the other hand the signal beam is monitored as a whole and the detected number of signal photons is used for post-selection.

The paper is organized as follows. Experimental setup is discussed in Sec. 2. Reconstruction of the experimental histograms using maximum-likelihood method and best fit by a multi-mode Gaussian field is described in Sec. 3. In Sec. 3, also the quantities used to characterize the post-selected fields including their nonclassicality are introduced. Properties of the fields post-selected by real detection are investigated in Sec. 4. The properties of the fields arising in ideal post-selecting detection are discussed in Sec. 5 using the experimental data and their complete reconstruction. Conclusions are drawn in Sec. 6.

2 Experimental setup

The schematic of the experimental setup is shown in Fig. 1(a). The light from the laser enters the frequency tripler. The TWB is generated in type-I spontaneous parametric down-conversion in a β -barium-borate crystal (BaB_2O_4 , BBO). Both beams of the TWB are detected by an iCCD camera as shown in Fig. 1(b). An interference bandpass filter is placed in front of the camera. The signal and idler beams produce stripes on the photocathode of the iCCD. The area in which the idler beam is detected is divided into three nearly equal parts. This forms a triple TWB with common detection in the signal beam.

The femtosecond cavity-dumped Ti:sapphire laser with the central wavelength of 840 nm serves as a light source. The wavelength at the output of the frequency tripler is 280 nm. The laser system repetition rate is 50 kHz and the pulse energy is 20 nJ. The iCCD camera Andor DH345-18U-63 has the detection-window width of 7 ns and is controlled by the synchronization pulses from the laser. The camera's sampling frequency is approximately 14 Hz. The bandpass interference filter F in front of the camera has the spectral width of 14 nm at the central wavelength of 560 nm. The pump intensity, and thus the TWB's intensity is actively stabilized using the detector D, motorized half-wave plate HWP, and polarization beam-splitter PBS.

Performing 1×10^6 measurement repetitions we have arrived at the experimental photocount histogram $f(c_s, c_{i_1}, c_{i_2}, c_{i_3})$ whose analysis gives comprehensive information about the field properties.

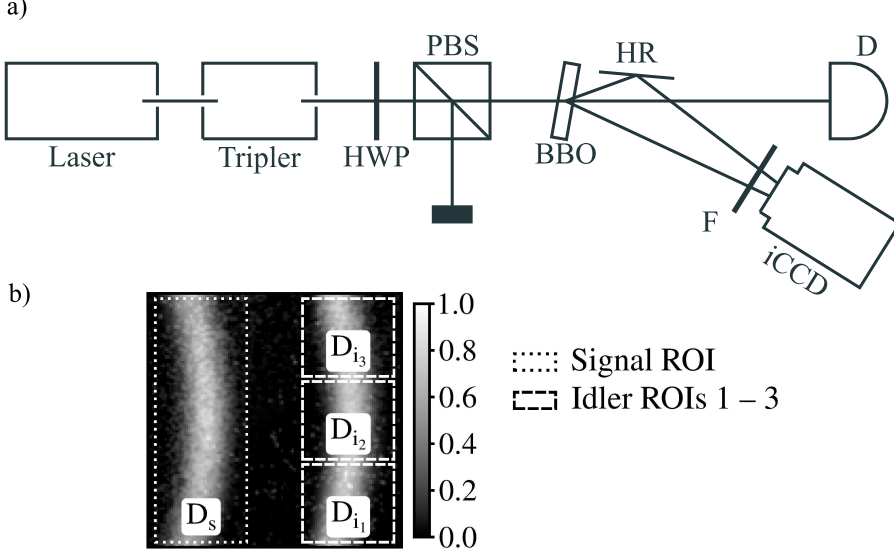


Figure 1: (a) Schematic of the experimental setup composed of laser, tripler, half-wave-plate HWP, polarizing beam splitter PBS, BBO crystal, highly-reflected mirror HR, laser-light detector D, frequency filter F, and iCCD camera. (b) Multiple exposition of an image acquired by the detector - (left) signal strip monitored by detector D_s , (right) idler strip divided into three parts detected by detectors D_{i1} , D_{i2} , and D_{i3} .

3 Reconstruction of the field

In the experimental four-dimensional (4D) photocount histogram $f(c_s, c_{i1}, c_{i2}, c_{i3})$, the value $f(c_s, c_{i1}, c_{i2}, c_{i3})$ gives the probability of detecting c_s , c_{i1} , c_{i2} , and c_{i3} photocounts in, in turn, the detection areas D_s , D_{i1} , D_{i2} , and D_{i3} . In the reconstruction we reveal a 4D photon-number distribution $p(n_s, n_{i1}, n_{i2}, n_{i3})$ that describes the common state of three multi-mode TWBs using the known detector characteristics. The field reconstruction can symbolically be illustrated as follows

$$f(c_s, c_{i1}, c_{i2}, c_{i3}) \longrightarrow p(n_s, n_{i1}, n_{i2}, n_{i3}). \quad (1)$$

Modelling the process of photon detection we express the photocount distribution f as a suitable linear function of photon-number distribution p [19] and this relation has to be inverted using suitable approach, e.g. by applying the maximum-likelihood (ML) approach. We note that if the used detector were ideal, i.e., its detection efficiency were 100% and it had no dark counts, the arrow in Eq. (1) would be replaced by an equal sign.

In addition to the reconstruction indicated in Eq. (1), it is possible to perform the following partial reconstruction

$$f(c_{i1}, c_{i2}, c_{i3}; c_s) \longrightarrow p(n_{i1}, n_{i2}, n_{i3}; c_s). \quad (2)$$

In this case, we fix the number c_s of post-selected signal photocounts and reconstruct the corresponding three-dimensional (3D) photon-number distribution. Thus, we reveal the 3D photon-number distributions of the optical fields directly present in the experimental setup.

Analogs of these 3D photon-number distributions appropriate for an ideal post-selecting detector are obtained from the reconstructed 4D photon-number distribution in Eq. (1).

We have applied two approaches to reconstruct the photon-number distributions in Eqs. (1) and (2). The first one is based upon a suitable Gaussian fit of the three original TWBs. [20, 21, 22, 17] The second method applies the ML approach. [17]

In the Gaussian-fit reconstruction, we consider three TWBs together and the photon-number distribution p_p of their common TWB composed of a paired and a noisy parts. The paired part of the distribution is given as the convolution of three paired parts belonging to individual TWBs:

$$p_p(n_s, n_{i1}, n_{i2}, n_{i3}) = \sum_{n_{s1}} \sum_{n_{s2}}^{n_s - n_{s1}} p_{p1}(n_{s1}, n_{i1}) p_{p2}(n_{s2}, n_{i2}) p_{p3}(n_s - n_{s1} - n_{s2}, n_{i3}), \quad (3)$$

Table 1: Detector properties.

property	D_s	$D_{i_1}, D_{i_2}, D_{i_3}$
number of active pixels	4536	1512
detection efficiency	0.233	0.226
dark count rate	0.220	0.073

Table 2: Parameters of the field reconstructed by the multi-mode Gaussian field.

component of field	subscript	B	M	$\langle n \rangle$
pairs s, i_1	p_1	0.00475	552	2.62
pairs s, i_2	p_2	0.0910	29.9	2.71
pairs s, i_3	p_3	0.0524	51.5	2.70
noise s	n_s	9.04	0.00779	0.070
noise i_1	n_{i_1}	3.28	0.0274	0.089
noise i_2	n_{i_2}	402	$6.33 \cdot 10^{-5}$	0.00025
noise i_3	n_{i_3}	10.9	0.00225	0.024

where p_{p_j} represent multi-mode thermal Mandel-Rice distributions of photon pairs $p_{p_j}(n_{s_j}, n_{i_j}) = \delta_{n_{s_j}, n_{i_j}} p^{M-R}(n_{s_j}; M_{p_j}, B_{p_j})$ for δ being the Kronecker symbol and label j indexing the TWBs, i.e. $j = 1, 2, 3$. The multi-mode thermal Mandel-Rice distribution takes the form

$$p^{M-R}(n; M, B) = \frac{\Gamma(n+M)}{n! \Gamma(M)} \frac{B^n}{(1+B)^{n+M}}, \quad (4)$$

in which M means the number of modes and B denotes the mean number of photons per mode.

To arrive at the Gaussian fit of the reconstructed photon-number distribution, the paired part in Eq. (3) has to be convolved with the noise part represented by the following four noise distributions

$$p(n_s, n_{i_1}, n_{i_2}, n_{i_3}) = \sum_{l_s=0}^{n_s} p_{n_s}(n_s - l_s) \sum_{l_{i_1}=0}^{n_{i_1}} p_{n_{i_1}}(n_{i_1} - l_{i_1}) \sum_{l_{i_2}=0}^{n_{i_2}} p_{n_{i_2}}(n_{i_2} - l_{i_2}) \sum_{l_{i_3}=0}^{n_{i_3}} p_{n_{i_3}}(n_{i_3} - l_{i_3}) p_p(l_{i_1}, l_{i_2}, l_{i_3}, l_s). \quad (5)$$

The noise photon-number distributions $p_{n_{i_j}}$ and p_{n_s} for $j = 1, 2, 3$ introduced in Eq. (5) are also described by their corresponding Mandel-Rice distributions in Eq. (4). All-together, the reconstructed photon-number distribution p is described by 14 parameters introduced above: $M_{p_1}, M_{p_2}, M_{p_3}, M_{n_s}, M_{n_{i_1}}, M_{n_{i_2}}, M_{n_{i_3}}, B_{p_1}, B_{p_2}, B_{p_3}, B_{n_s}, B_{n_{i_1}}, B_{n_{i_2}},$ and $B_{n_{i_3}}$. They are determined [20, 22], together with the corresponding detection efficiencies, from the requirement of equal first- and second-order intensity (photocount) moments taken from the experiment and the Gaussian theoretical fit and minimal declination between the experimental histogram and its theoretical prediction.

Using the experimental data and detector parameters as summarized in Table 1, we obtain the values of 14 parameters that characterize the distribution $p(n_s, n_{i_1}, n_{i_2}, n_{i_3})$. These parameters are summarized in Table 2.

On the other hand, the ML reconstruction method [23, 24] is iterative and starts with a uniform distribution. After suitable number of steps the iteration approaches its steady state that gives us the looked-for photon-number distribution (for details, see [25]).

Then, the set of partially reconstructed distributions (for fixed c_s) $p(n_{i_1}, n_{i_2}, n_{i_3}; c_s)$, as described in Eq. (2), is derived along the formula

$$p(c_s, n_{i_1}, n_{i_2}, n_{i_3}) = \sum_{n_s=0}^{\infty} T(c_s, n_s) p(n_s, n_{i_1}, n_{i_2}, n_{i_3}), \quad (6)$$

where the detection matrix $T(c_s, n_s)$ gives the probability that c_s photocounts are detected when n_s photons arrive at the detector (for details, see, e.g., Ref. [25]). The elements of the detection matrix T depend on the properties of the detector, namely the number of active pixels, detection efficiency, and dark-count rate.

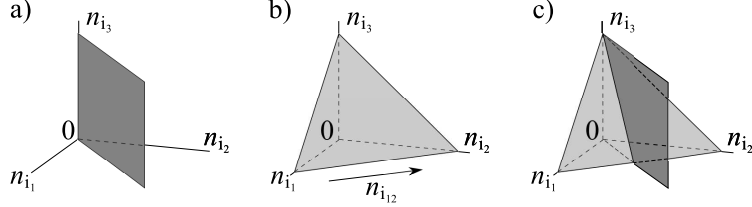


Figure 2: Graphical representation of diagonal and triangular planes in the space $(n_{i_1}, n_{i_2}, n_{i_3})$: (a) diagonal plane, (b) triangular plane, (c) both planes.

The 3D photon-number distributions $p_{c_s}(n_{i_1}, n_{i_2}, n_{i_3})$ and $p_{n_s}(n_{i_1}, n_{i_2}, n_{i_3})$ characterizing the fields post-selected by detecting c_s signal photocounts (real detection) and n_s signal photons (ideal detection) are derived from the above 4D photon-number distributions by appropriate normalization:

$$p_{c_s}(n_{i_1}, n_{i_2}, n_{i_3}) = p(c_s, n_{i_1}, n_{i_2}, n_{i_3}) / \sum_{n_{i_1}, n_{i_2}, n_{i_3}} p(c_s, n_{i_1}, n_{i_2}, n_{i_3}), \quad (7)$$

$$p_{n_s}(n_{i_1}, n_{i_2}, n_{i_3}) = p(n_s, n_{i_1}, n_{i_2}, n_{i_3}) / \sum_{n_{i_1}, n_{i_2}, n_{i_3}} p(n_s, n_{i_1}, n_{i_2}, n_{i_3}). \quad (8)$$

The corresponding 3D photocount histograms are determined as

$$f_{c_s}(c_{i_1}, c_{i_2}, c_{i_3}) = f(c_s, c_{i_1}, c_{i_2}, c_{i_3}) / \sum_{c_{i_1}, c_{i_2}, c_{i_3}} f(c_s, c_{i_1}, c_{i_2}, c_{i_3}). \quad (9)$$

We note that below we represent the main features of the reconstructed post-selected 3D photon-number distributions p_{n_s} and p_{c_s} using two representative planes (cuts) in the whole 3D space spanned by the photon-numbers n_{i_1} , n_{i_2} , and n_{i_3} . These 'diagonal' and 'triangular' planes are shown in Fig. 2. For clarity, coordinate $n_{i_{12}}$ is used to describe triangular planes, the meaning of which is shown in Fig. 2(b).

Sub-Poissonianity of the post-selected beams is quantified using the Fano factor

$$F_{n_{i_j}} = \frac{\langle (\Delta n_{i_j})^2 \rangle}{\langle \Delta n_{i_j} \rangle}, \quad (10)$$

where $\langle (\Delta n)^2 \rangle \equiv \langle n^2 \rangle - \langle n \rangle^2$ and $\langle n^k \rangle$ gives a k -th photon-number moment.

Anti-correlations between the photon-number fluctuations Δn_{i_j} and Δn_{i_k} in the j -th and k -th idler beams are quantified by negative values of the following correlation function

$$C_{\Delta n_{i_j} i_k} = \frac{\langle \Delta n_{i_j} \Delta n_{i_k} \rangle}{\sqrt{\langle (\Delta n_{i_j})^2 \rangle \langle (\Delta n_{i_k})^2 \rangle}}. \quad (11)$$

Nonclassicality of the post-selected 3D idler fields is revealed by suitable nonclassicality criteria (NCCa). The NCCa are typically written as mathematical inequalities whose fulfillment guarantees the field nonclassicality. [26] The NCCa inequalities are often written in terms of the moments of integrated intensities. [27] There exist a large number of various moment NCCa [27, 28] derived by specific approaches and suitable for specific kinds of fields. The nonclassicality of the fields built up from twin beams is efficiently detected by the Cauchy-Schwarz and matrix NCCa. [26]

In our analysis, we apply the moment Cauchy-Schwarz NCC referred to as C_{111}^{000} and defined as

$$C_{111}^{000} = \langle W_{i_1}^2 W_{i_2}^2 W_{i_3}^2 \rangle - \langle W_{i_1} W_{i_2} W_{i_3} \rangle^2 < 0 \quad (12)$$

using the moments of intensities W_{i_1} , W_{i_2} , and W_{i_3} associated in turn with the photon-numbers n_{i_1} , n_{i_2} , and n_{i_3} and characterizing the field intensities at the detectors D_{i_1} , D_{i_2} , and D_{i_3} . In parallel, we also use the intensity matrix NCC referred to as $M_{101\ 010\ 000}$ and given by the formula

$$\begin{aligned} M_{101\ 010\ 000} &= \langle W_{i_1}^2 W_{i_3}^2 \rangle \langle W_{i_2}^2 \rangle + 2 \langle W_{i_1} W_{i_2} W_{i_3} \rangle \langle W_{i_2} \rangle \langle W_{i_1} W_{i_3} \rangle \\ &\quad - \langle W_{i_1} W_{i_3} \rangle^2 \langle W_{i_2}^2 \rangle - \langle W_{i_2} \rangle^2 \langle W_{i_1}^2 W_{i_3}^2 \rangle - \langle W_{i_1} W_{i_2} W_{i_3} \rangle^2 < 0. \end{aligned} \quad (13)$$

The moment NCCa can be transformed into their probability counterparts using the Mandel detection formula. [26, 28] The corresponding inequalities are expressed in terms of probabilities of photon-number distributions. As examples, we express the probability NCCa \bar{C}_{111}^{000} and $\bar{M}_{101\ 010\ 000}$ corresponding to the intensity NCCa given in Eqs. (12) and (13):

$$\bar{C}_{111}^{000} = 8p_{c/n}(0, 0, 0)p_{c/n}(2, 2, 2) - [p_{c/n}(1, 1, 1)]^2 < 0, \quad (14)$$

$$\begin{aligned} \bar{M}_{101\ 010\ 000} = & (2!)^3 p_{c/n}(2, 0, 2)p_{c/n}(0, 2, 0)p_{c/n}(0, 0, 0) \\ & + 2p_{c/n}(1, 1, 1)p_{c/n}(0, 1, 0)p_{c/n}(1, 0, 1) \\ & - 2![p_{c/n}(1, 0, 1)]^2 p_{c/n}(0, 2, 0) - (2!)^2 [p_{c/n}(0, 1, 0)]^2 p_{c/n}(2, 0, 2) \\ & - [p_{c/n}(1, 1, 1)]^2 p_{c/n}(0, 0, 0) < 0. \end{aligned} \quad (15)$$

In Eq. (15), we substitute for $p_{c/n}$ either p_{c_s} or p_{n_s} [Eqs.(7), (8)] depending on whether the post-selection is performed according to the number of photocounts or photons. General formulation of probability NCCa and details can be found in Refs. [27, 28, 26].

The NCCa not only identify the nonclassicality, they also provide their quantification using the Lee nonclassicality depth (NCD). [29] The NCD τ is derived from the threshold value s_{th} of the ordering parameter at which the corresponding quasi-distribution P of integrated intensities begins to behave as a classical distribution observed by a given NCC:

$$\tau = (1 - s_{\text{th}})/2. \quad (16)$$

To determine the threshold value of s_{th} the moments of integrated intensities as well as the photon-number distributions have to be transformed to their general s -ordered forms. [19]

Using probability NCCa, we construct below 3D fields $\bar{\tau}(n_{i_1}, n_{i_2}, n_{i_3})$ of NCDs. To determine the value of NCD $\bar{\tau}$ at specific point $(n_{i_1}, n_{i_2}, n_{i_3})$, we consider only those NCCa that contain the probabilities in the closest neighborhood of this point and take the greatest value of the obtained NCDs. The 3D fields $\bar{\tau}(n_{i_1}, n_{i_2}, n_{i_3})$ of NCDs are then plotted in their diagonal and triangular planes.

4 Post-selection with real detector

We analyze the experimental 3D photocount histograms $f(n_{i_1}, n_{i_2}, n_{i_3}; c_s)$ considered as a function of the number c_s of post-selecting signal photocounts and assign to them the photon-number distribution $p_i^{\text{ML}}(n_{i_1}, n_{i_2}, n_{i_3}; c_s)$ obtained by ML method and the photon-number distribution $p_i^G(n_{i_1}, n_{i_2}, n_{i_3}; c_s)$ arising from the multi-mode Gaussian fit.

The post-selected idler fields are characterized by their mean photon numbers $\langle n_{i_j} \rangle$ in an idler field, their Fano factors $F_{n_{i_j}}$, and their correlation functions $C_{\Delta n_{i_j} i_k}$ between two idler fields. We note that, in our fields, the mean numbers of the idler fields, their Fano factors, and correlation functions behave similarly in all three idler fields.

According to Fig. 3(a), the mean photon numbers $\langle n_{i_1} \rangle$ increase with the increasing signal photocount number c_s . On the other hand, the Fano factors F_{i_1} decrease with the increasing c_s up to $c_s = 7$ and then they increase, as shown in Fig. 3(b). Similar behavior is observed in Fig. 3(c) for the correlation function $C_{\Delta n_{i_2} i_3}$ that exhibits an increase of anti-correlations between the idler beams 2 and 3 with the increasing c_s up to $c_s = 7$ and then this anti-correlation weakens. Such behavior reflects nonunit detection efficiency of the post-selecting detector and its nonzero dark-count rate. [11, 17] Whereas nonunit detection efficiency has particularly negative influence at the Fano factor $F_{n_{i_1}}$ and correlation function $C_{\Delta n_{i_2} i_3}$ at low post-selecting signal photocount numbers c_s , nonzero dark-count rate negatively affect the post-selection mechanism at higher photocount numbers c_s .

To illustrate typical properties of the reconstructed fields, we draw in Figs. 4(a,b) the photon-number distribution $p_i^{\text{ML}}(n_{i_1}, n_{i_2}, n_{i_3}) \equiv p_{c_s=5}^{\text{ML}}(n_{i_1}, n_{i_2}, n_{i_3})$ of the field post-selected by detecting $c_s = 5$ signal photocounts in its diagonal and triangular planes. Nonclassicality of this field is certified directly from the form of its quasi-distribution $P_i^{\text{ML}}(W_{i_1}, W_{i_2}, W_{i_3})$ of intensities drawn in Figs. 4(c,d) for the ordering parameter $s = 0.05$. [17] In Figs. 4(c,d), regions with negative probabilities located between the axes and the area with the maximal probabilities are apparent. This quasi-distribution determined as $s = 0.05$ means that the true value of the NCD τ is greater than 0.475. We compare this value of NCD τ with those suggested by the probability Cauchy–Schwarz NCCa and the matrix NCCa whose NCDs $\bar{\tau}$ are drawn in Figs. 5(a–d) as they depend on the location in the space of the idler-beam photon numbers $(n_{i_1}, n_{i_2}, n_{i_3})$. Whereas the maximal NCD $\bar{\tau}_C = 0.45$ in the case of the Cauchy–Schwarz NCCa, the matrix NCCa provides the greater maximal NCD $\bar{\tau}_M = 0.56$ certifying its better performance. [17]. Better performance of the matrix NCCa compared to their Cauchy–Schwarz counterparts is observed also when we apply the corresponding intensity NCCa C_{111}^{000} ($\tau_C = 0.00$) and $M_{101\ 010\ 000}$ ($\tau_M = 0.12$) given in Eqs. (12) and (13). However, the achieved values of NCDs τ are considerably smaller than when the probability NCCa are applied; the intensity Cauchy–Schwarz NCC even does not indicate the nonclassicality.

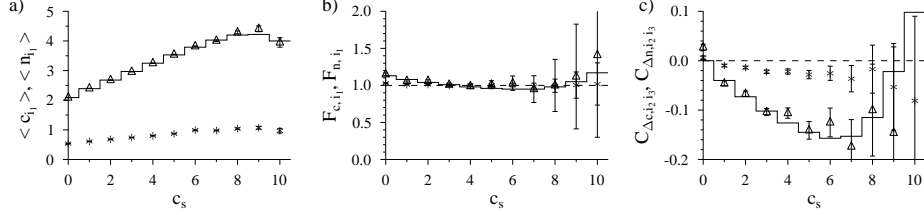


Figure 3: (a) Mean photon (photocount) number $\langle n_{i_1} \rangle$ ($\langle c_{i_1} \rangle$) of idler beam 1, (b) its Fano factor F_{n,i_1} (F_{c,i_1}), and (c) correlation function $C_{\Delta n_{i_2} i_3}$ [$C_{\Delta c_{i_2} i_3}$] of photon-number fluctuations in idler beams 2 and 3 as they depend on the post-selecting signal photocount number c_s . Symbols $*$ belong to the experimental photocount histogram, symbols \triangle to ML reconstruction, and solid curves to Gaussian reconstruction.

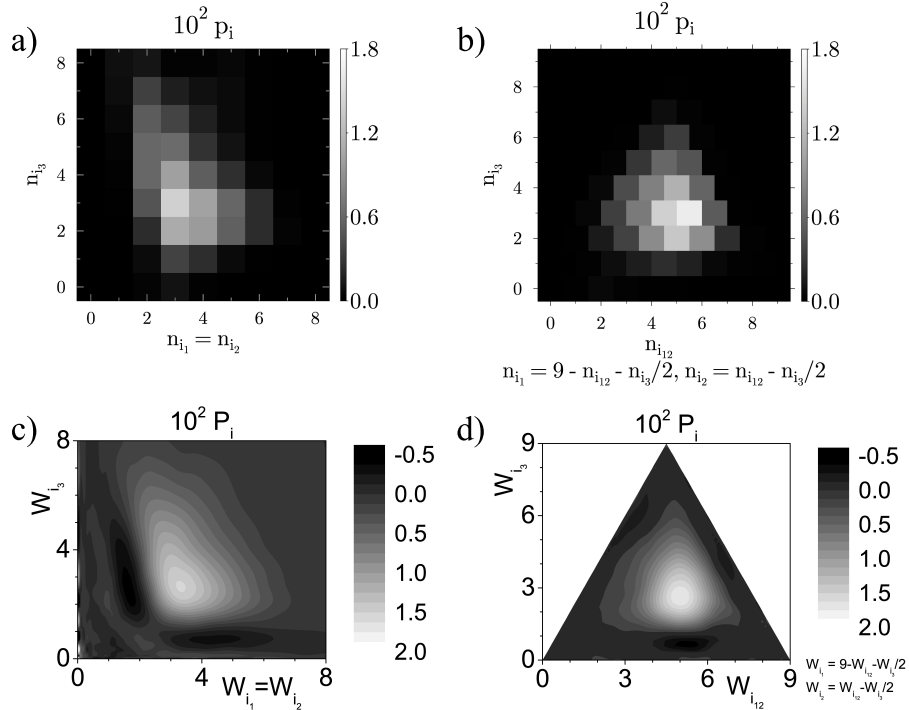


Figure 4: Photon-number distribution $p_i^{\text{ML}}(n_{i_1}, n_{i_2}, n_{i_3})$ drawn in its (a) diagonal and (b) triangular planes and quasi-distribution $P_i^{\text{ML}}(W_{i_1}, W_{i_2}, W_{i_3})$ of integrated intensities drawn in its (c) diagonal and (d) triangular planes for the field reached by real post-selection with $c_s = 5$.

5 Post-selection with ideal detector

Marginal sub-Poissonianity and anti-correlations of photon-number fluctuations of the idler beams represent the prominent features of the post-selected fields. Nevertheless, to observe them the signal-beam detector used for post-selection has to have sufficiently high detection efficiency. This is the reason why the post-selected experimental idler fields did not exhibit their sub-Poissonianity. To demonstrate the general features of these states available by using sufficiently efficient detectors in connection with the measured experimental histogram, we make complete reconstruction of the 4D photon-number distribution $p(n_s, n_{i_1}, n_{i_2}, n_{i_3})$ using the measured histogram $f(c_s, c_{i_1}, c_{i_2}, c_{i_3})$. Then, fixing the number n_s of signal photons, we are left with the conditional photon-number distribution $p_{n_s}(n_{i_1}, n_{i_2}, n_{i_3})$. Such distribution corresponds to the experimental situation in which an ideal detector is used for post-selection. Similarly as above in Sec. 4, we use the iterative ML method and the Gaussian fit for reconstruction.

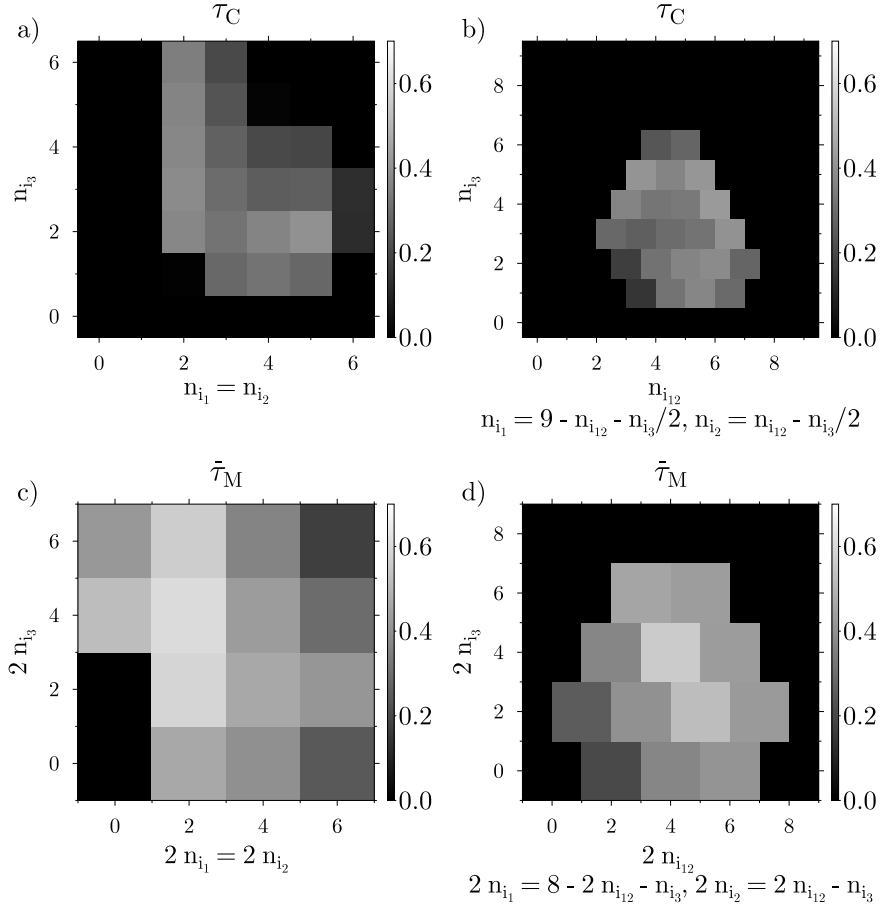


Figure 5: Nonclassicality depth $\bar{\tau}_C$ [$\bar{\tau}_M$] for the probability Cauchy–Schwarz [matrix] NCCa drawn in its (a) [(c)] diagonal and (b) [(d)] triangular planes for the field reached by real post-selection assuming $c_s = 5$.

The mean number $\langle n_{i_1} \rangle$ of photons in the idler beam 1 increases approximately linearly with the number n_s of post-selecting signal photons and we approximately have $\langle n_{i_1} \rangle \approx n_s/3$ [see Fig. 6(a)]. Importantly, the Fano factors F_{i_1} decrease with the increasing number n_s of post-selecting signal photons up to $n_s = 13$ and attain their values lower than 0.8 [see Fig. 6(b)], which is considerably lower than the quantum-classical border 1. Also the correlation function $C_{\Delta n_{i_2} i_3}$ of photon-number fluctuations between the idler beams 2 and 3 attains minimal negative values less than -0.45, indicating strong anti-correlations [see Fig. 6(c)].

To demonstrate the properties of the analyzed fields in their most general form, we plot in Figs. 7(a,b) as an example the photon-number distribution $p_i^{\text{ML}}(n_{i_1}, n_{i_2}, n_{i_3}) \equiv p_{n_s=10}^{\text{ML}}(n_{i_1}, n_{i_2}, n_{i_3})$ of the field post-selected by detecting $n_s = 10$ signal photons in its diagonal and triangular planes in the form obtained by the ML reconstruction. The corresponding quasi-distribution $P_i^{\text{ML}}(W_{i_1}, W_{i_2}, W_{i_3})$ of integrated intensities calculated for $s = 0$ are shown in Figs. 7(c,d) in their diagonal and triangular planes for comparison. Negative regions in these graphs mean that the true value of NCD τ is greater than 0.5. Comparing the graphs of quasi-distributions P_i^{ML} drawn in Figs. 4(c,d) and 7(c,d) for the idler fields reached by real and ideal post-selection, respectively, quality of the reconstructed quasi-distribution P_i^{ML} obtained with ideal post-selecting detector is much better. This also results in greater values of the NCDs τ belonging to both the probability and intensity NCCa. The NCDs $\bar{\tau}_C$ obtained from the Cauchy–Schwarz NCCa are drawn in Figs. 8(a,b), whereas the NCDs $\bar{\tau}_M$ of the matrix NCCa are plotted in Figs. 8(c,d). The reached maximal values of NCDs $\bar{\tau}$, $\bar{\tau}_C = 0.56$ and $\bar{\tau}_M = 0.65$, are greater than those reached by real post-selection and belonging to the idler field post-selected by $c_s = 5$ signal photons analyzed in Sec. 4. Though the intensity Cauchy–Schwarz NCC C_{111}^{000} and matrix NCC $M_{101\ 010\ 000}$ are less efficient than their probability counterparts, they provide much higher values of NCDs τ , $\tau_C = 0.36$ and $\tau_M = 0.38$ compared to the case analyzed in Sec. 4.

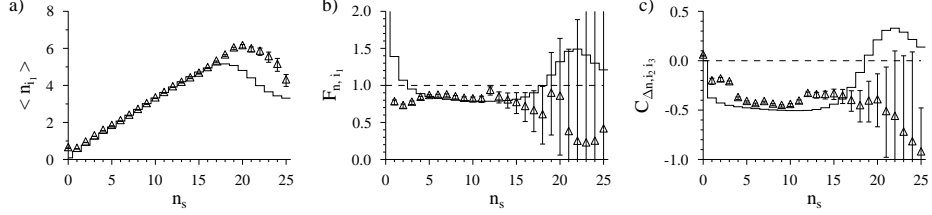


Figure 6: (a) Mean photon number $\langle n_{i1} \rangle$ of idler beam 1, (b) its Fano factor $F_{n,i1}$, and (c) correlation function $C_{\Delta n,i2 i3}$ of photon-number fluctuations in idler beams 2 and 3 as they depend on the post-selecting signal photon number n_s using ideal signal-beam detector. Symbols \triangle originate in ML reconstruction and solid curves arise in Gaussian reconstruction.

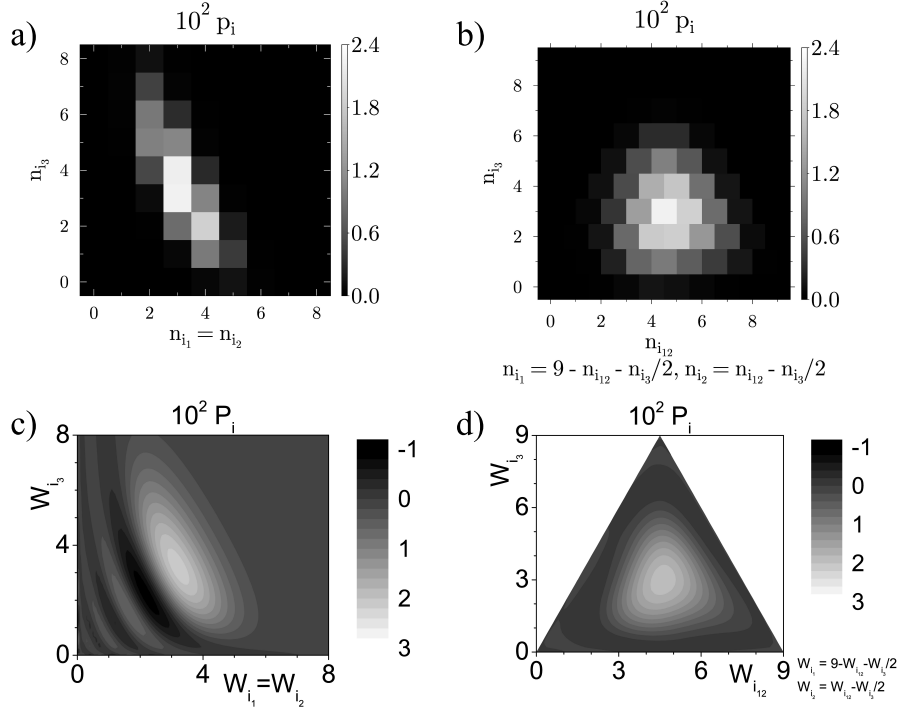


Figure 7: Photon-number distribution $p_i^{\text{ML}}(n_{i1}, n_{i2}, n_{i3})$ drawn in its (a) diagonal and (b) triangular planes and quasi-distribution $P_i^{\text{ML}}(W_{i1}, W_{i2}, W_{i3})$ of integrated intensities drawn in its (c) diagonal and (d) triangular planes for the idler field reached by ideal post-selection assuming $n_s = 10$.

6 Conclusions

Using photon-number- and spatially- resolved detection of a twin beam as provided by an iCCD camera we have obtained specific three-beam states exhibiting mutual anti-correlations in photon-number fluctuations of the beams and marginal sub-Poissonian photon-number distributions. These states arise after photon-number-resolved post-selection in a common signal beam whose idler counterpart is divided into three spatially separated idler beams of comparable intensity. Nonclassicality of the post-selected fields is certified using suitable intensity and probability nonclassicality criteria and their accompanying nonclassicality depths as well as quasi-distributions of integrated intensities. The Fano factor quantifies sub-Poissonianity of the marginal beams. The properties of the states obtained by using both real and ideal post-selecting detectors are analyzed and mutually compared.

Whereas the states obtained by ideal post-selection exhibit both anti-correlations in photon-number fluctuations and marginal sub-Poissonianity, lower detection efficiency of the real post-selecting detector concealed the marginal sub-Poissonianity. Nevertheless, the nonclassicality of the three-beam states dominantly reflects the quantum correlations.

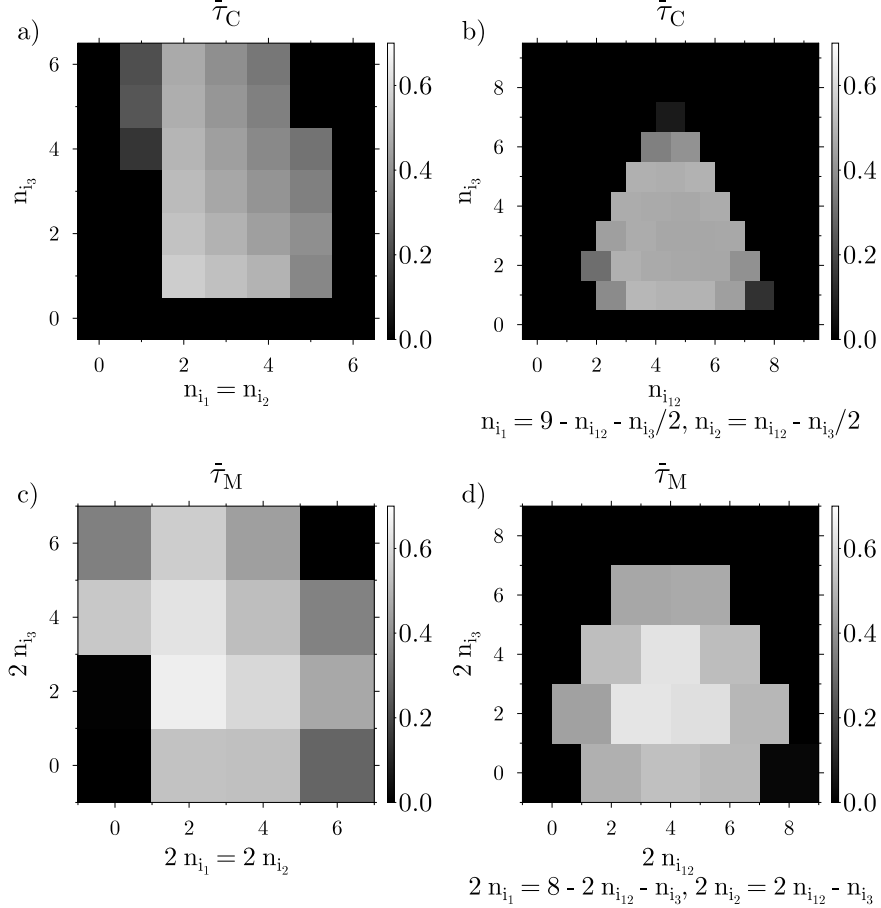


Figure 8: Nonclassicality depth $\bar{\tau}_C$ [$\bar{\tau}_M$] for the probability Cauchy–Schwarz [matrix] NCCa drawn in its (a) [(c)] diagonal and (b) [(d)] triangular planes for the field reached by ideal post-selection assuming $n_s = 10$.

These are strong both when real and ideal post-selection is applied. Quantum correlations are substantial for application potential of these states.

The generated states are potentially useful for metrology applications and well as for different quantum-information protocols, e.g. in the area of secure-quantum communications.

Acknowledgments

The authors acknowledge support by the project OP JAC CZ.02.01.01/00/22_008/0004596 of the Ministry of Education, Youth, and Sports of the Czech Republic.

References

- [1] Boyd R W 2003 *Nonlinear Optics*, 2nd edition (Academic Press, New York)
- [2] Mandel L and Wolf E 1995 *Optical Coherence and Quantum Optics* (Cambridge University, Cambridge)
- [3] Genovese M 2016 *J. Opt.* **18** 073002
- [4] Jedrkiewicz O, Jiang Y K, Brambilla E, Gatti A, Bache M, Lugiato L A and Di Trapani P 2004 *Phys. Rev. Lett.* **93** 243601
- [5] Haderka O, Peřina Jr J, Hamar M and Peřina J 2005 *Phys. Rev. A* **71** 033815
- [6] Bondani M, Allevi A, Zambra G, Paris M G A and Andreoni A 2007 *Phys. Rev. A* **76** 013833

- [7] Blanchet J L, Devaux F, Furfaro L and Lantz E 2008 *Phys. Rev. Lett.* **101** 233604
- [8] Rarity J and Tapster P 1997 *Phil. Trans. R. Soc. Lond. A* **355** 2267—2277
- [9] Laurat J, Coudreau T, Treps N, Maitre A and Fabre C 2003 *Phys. Rev. Lett.* **91** 213601
- [10] Zou H, Zhai S, Guo J, Yang R and Gao J 2006 *Opt. Lett.* **31** 1735—1737
- [11] Peřina Jr J, Haderka O and Michálek V 2013 *Opt. Express* **21** 19387—19394
- [12] Lamperti M, Allevi A, Bondani M, Machulka R, Michálek V, Haderka O and Peřina Jr J 2014 *J. Opt. Soc. Am. B* **31** 20—25
- [13] Iskhakov T S, Usenko V C, Andersen U L, Filip R, Chekhova M V and Leuchs G 2016 *Opt. Lett.* **41** 2149—2152
- [14] Harder G, Bartley T J, Lita A E, Nam S W, Gerrits T and Silberhorn C 2016 *Phys. Rev. Lett.* **116** 143601
- [15] Jakeman E and Rarity J G 1986 *Opt. Commun.* **59** 219—223
- [16] Sabines-Chesterkind J, McMillan A R, Moreau P A, Josh S K, Knauer S, Johnston E, Rarity J G and Matthews J C F 2019 *Opt. Express* **27** 30810—30818
- [17] Peřina Jr J, Michálek V, Machulka R and Haderka O 2021 *Phys. Rev. A* **104** 013712
- [18] Peřina Jr J, Michálek V, Machulka R and Haderka O 2021 *Opt. Express* **29** 29704
- [19] Peřina J 1991 *Quantum Statistics of Linear and Nonlinear Optical Phenomena* (Kluwer, Dordrecht)
- [20] Peřina Jr J, Haderka O, Hamar M and Michálek V 2012 *Opt. Lett.* **37** 2475—2477
- [21] Peřina Jr J 2013 *Phys. Rev. A* **87** 013833
- [22] Peřina Jr J, Haderka O, Michálek V and Hamar M 2013 *Phys. Rev. A* **87** 022108
- [23] Dempster A P, Laird N M and Rubin D B 1977 *J. Royal Statist. Soc. B* **39** 1—38
- [24] Vardi Y and Lee D 1993 *J. Royal Statist. Soc. B* **55** 569—612
- [25] Peřina Jr J, Hamar M, Michálek V and Haderka O 2012 *Phys. Rev. A* **85** 023816
- [26] Peřina Jr J, Pavliček P, Michálek V, Machulka R and Haderka O 2022 *Phys. Rev. A* **105** 013706
- [27] Peřina Jr J, Arkhipov I I, Michálek V and Haderka O 2017 *Phys. Rev. A* **96** 043845
- [28] Peřina Jr J, Haderka O and Michálek V 2020 *Phys. Rev. A* **102** 043713
- [29] Lee C T 1991 *Phys. Rev. A* **44** R2775—R2778